

PCCP

Accepted Manuscript

This article can be cited before page numbers have been issued, to do this please use: S. Aškrabi, V. D. D. Araújo, M. Passacantando, M. Basso, N. Tomi, B. Dojcinovic, D. Manojlovic, B. Calija, M. Mileti and Z. D. Dohevi-Mitrovi, *Phys. Chem. Chem. Phys.*, 2017, DOI: 10.1039/C7CP06440C.



This is an Accepted Manuscript, which has been through the Royal Society of Chemistry peer review process and has been accepted for publication.

Accepted Manuscripts are published online shortly after acceptance, before technical editing, formatting and proof reading. Using this free service, authors can make their results available to the community, in citable form, before we publish the edited article. We will replace this Accepted Manuscript with the edited and formatted Advance Article as soon as it is available.

You can find more information about Accepted Manuscripts in the [author guidelines](#).

Please note that technical editing may introduce minor changes to the text and/or graphics, which may alter content. The journal's standard [Terms & Conditions](#) and the ethical guidelines, outlined in our [author and reviewer resource centre](#), still apply. In no event shall the Royal Society of Chemistry be held responsible for any errors or omissions in this Accepted Manuscript or any consequences arising from the use of any information it contains.



Journal Name

ARTICLE

Nitrate-assisted photocatalytic efficiency of defective Eu-doped Pr(OH)₃ nanostructures

S. Aškračić,^a V. D. Araujo,^b M. Passacantando,^c M. I. B. Bernardi,^d N. Tomić,^a B. Dojčinović,^e D. Manojlović,^f B. Čalić,^g M. Miletić^a and Z. D. Dohčević-Mitrović^{*a}

Received 00th January 20xx,
Accepted 00th January 20xx

DOI: 10.1039/x0xx00000x

www.rsc.org/

Pr(OH)₃ one dimensional nanostructures present less studied member of lanthanide hydroxides which recently demonstrated excellent adsorption capacity for organic pollutant removal from wastewater. In this study Pr_{1-x}Eu_x(OH)₃ (x = 0, 0.01, 0.03, 0.05) defective nanostructures were synthesized by facile and scalable microwave-assisted hydrothermal method using KOH as alkaline metal precursor. The phase and surface composition, morphology, vibrational, electronic and optical properties of the as-prepared samples were characterized by X-ray diffraction (XRD), X-ray photoelectron spectroscopy (XPS), Inductively Coupled Plasma Optical Emission Spectrometry (ICP-OES), Transmission electron microscopy (TEM), Field emission scanning electron microscopy (FE-SEM), Raman, Infrared (IR), Photoluminescence (PL) and Diffuse reflectance spectroscopy (DRS). It was deduced that incorporation of Eu³⁺ ions promotes the formation of oxygen vacancies in already defective Pr(OH)₃, changing at the same time the Pr(OH)₃ nanorods morphology. The presence of KNO₃ phase was registered in Eu-doped samples. The oxygen-deficient Eu-doped Pr(OH)₃ nanostructures display improved photocatalytic activity in reactive orange (RO16) dye removal under UV-vis light irradiation. Enhanced photocatalytic activity of Eu-doped Pr(OH)₃ nanostructures is caused by synergetic effect of oxygen vacancies and Eu³⁺ (NO₃⁻) ions present on Pr(OH)₃ surface, on charge separation efficiency and formation of reactive radicals. In addition, 3% Eu-doped sample exhibited very good adsorptive properties due to different morphology and higher electrostatic attraction with anionic dye. Pr_{1-x}Eu_x(OH)₃ nanostructures with possibility of tuning their adsorption/photocatalytic properties present great potential for wastewater treatment.

Introduction

Nanocrystalline rare earth hydroxides have started to draw attention in the recent years because they are relatively facile to synthesize and usually do not require high temperature annealing. As all rare earth compounds, lanthanide hydroxides display interesting catalytic, optical, magnetic and adsorptive properties¹⁻⁵. They also represent straight forward approach for obtaining rare

earth oxides, since annealing at higher temperatures transforms these hydroxides to oxides. Rare earth hydroxides in the form of one dimensional nanostructures were synthesized by different methods such as precipitation, hydrothermal or microemulsion method or electrodeposition²⁻⁹. It is known that lanthanide hydroxides most often crystallize into one dimensional (1D) structures, such as nanorods, nanobundles or nanobelts. 1D porous structures have potential for application in water pollutant removal since their dimensionality makes them much more accessible to the pollutant molecules. On the other hand, it is expected that the abundance of -OH groups (inherent in these materials) can have significant impact on their photocatalytic and adsorptive properties. As 1D nanostructures are expected to have better surface activity if the total surface to volume ratio is higher, it is of interest to obtain nanorods/nanowires with high length-to-diameter ratio. 1D geometry (the aspect ratio of longer to shorter dimension) can be tuned in hydrothermal synthesis process by changing the molar ratios of [OH⁻]/[Ln³⁺], where OH⁻ ions originate from hydroxide precursor, and Ln³⁺ ions from lanthanide salt or oxide, but this ratio

^a Center for Solid State Physics and New Materials, Institute of Physics Belgrade, University of Belgrade, Pregrevica 118, 11080 Belgrade, Serbia. Email: sonask@ipb.ac.rs, zordoh@ipb.ac.rs

^b Unidade Acadêmica do Cabo de Santo Agostinho, Universidade Federal Rural de Pernambuco, Cabo de Santo Agostinho, PE, Brazil.

^c Department of Physical and Chemical Sciences, University of L'Aquila, Via Vetoio, 67100 Coppito L'Aquila, Italy.

^d Instituto de Física de São Carlos, Universidade de São Paulo, São Carlos, SP, Brazil.

^e Center of Chemistry, Institute of Chemistry, Technology and Metallurgy, University of Belgrade, Njegoševa 12, 11000 Belgrade, Serbia.

^f Faculty of Chemistry, University of Belgrade, Studentski trg 12-16, 11000 Belgrade, Serbia.

^g Faculty of Pharmacy, University of Belgrade, Vojvode Stepe 450, 11221 Belgrade, Serbia

is also dependent on the choice of alkaline metal hydroxide. In the case of $\text{Eu}(\text{OH})_3$ it was shown that with increasing ratio of $[\text{OH}^-]/[\text{Eu}^{3+}]$, the aspect ratio of the 1D nanostructures decreased when NaOH was used⁴, but increased when KOH was used¹⁰.

Among nanocrystalline lanthanide hydroxides, electrochemically prepared 1D $\text{Pr}(\text{OH})_3$ nanostructures were shown to possess excellent adsorptive properties regarding dye removal from water⁶. Electrodeposition was also used to produce 1D $\text{Pr}(\text{OH})_3$ nanostructures that demonstrated good adsorption of phosphates⁸. Furthermore, 1D porous $\text{Pr}(\text{OH})_3$ nanowire bundles synthesized by template-free electrochemical deposition method demonstrated good ferromagnetic properties². In addition, toxicity studies of porous $\text{Pr}(\text{OH})_3$ nanostructures demonstrated their great potential as environmentally friendly adsorbent materials⁷.

There is only a few papers dedicated to the investigation of 1D $\text{Pr}(\text{OH})_3$ nanostructures^{2, 6-9} and majority of them concerned adsorptive properties of this material. To the best of our knowledge, photocatalytic properties of pure or doped $\text{Pr}(\text{OH})_3$ have not been investigated up to present. This is probably due to the relatively large band gap of these materials (4.7 eV) and their consequent insufficient efficiency in absorption of the solar radiation. However, recent work by Dong et al³ showed that oxygen vacancies can create electronic states within the band gap of $\text{La}(\text{OH})_3$ nanorods, extending their photoresponse range and making them very efficient photocatalysts. In addition to this, doping of $\text{La}(\text{OH})_3$ nanorods with lanthanides, Ln^{3+} , improved drastically their photocatalytic activity, where Eu^{3+} was one of dopants that produced best results in this direction¹¹.

In this study $\text{Pr}(\text{OH})_3$ nanorods and $\text{Pr}_{1-x}\text{Eu}_x(\text{OH})_3$ ($x = 0.01, 0.03, 0.05$) nanostructures were obtained by microwave-assisted hydrothermal method. We demonstrated that Eu doping influences the changes in $\text{Pr}(\text{OH})_3$ morphology, adsorption affinity and can substantially increase the photocatalytic activity of $\text{Pr}(\text{OH})_3$ nanorods towards dye degradation. Additionally, the doping changes the content of oxygen vacancies, which, together with synthesis-introduced nitrates and morphology, determine whether the resulting nanostructures are dominantly photocatalysts or adsorbents. Facile and scalable synthesis, high photocatalytic activity of Eu-doped $\text{Pr}(\text{OH})_3$ nanostructures and the possibility of tuning the ratio of their adsorptive/photocatalytic activity present a great potential for their application in efficient and cost-effective pollutant removal.

Experimental

Preparation of pure and Eu-doped $\text{Pr}(\text{OH})_3$ nanostructures

$\text{Pr}_{1-x}\text{Eu}_x(\text{OH})_3$ ($x = 0, 0.01, 0.03, 0.05$) nanostructures were prepared by the microwave-assisted hydrothermal method, from the precursor oxides Pr_6O_{11} and Eu_2O_3 . The synthesis procedure included the following steps: firstly, precursors were dissolved in aqueous HNO_3 , subsequently, 0.02 mol of dissolved Pr- and Eu-precursors (0, 1%, 3% and 5% at. Eu) were added into 50 mL of distilled water. After that 50 mL of a 10 M KOH solution was added

rapidly under vigorous stirring. KOH was chosen as a precursor for hydrothermal synthesis of pure and doped $\text{Pr}(\text{OH})_3$ nanorods in this study, as it has been shown that it enhances formation of 1D nanorods with higher ratio of length to diameter¹⁰. The mixed solution was placed in a 110 mL Teflon autoclave (filling 90% of its volume) which was sealed and placed in a microwave assisted hydrothermal system, applying 2.45 GHz of microwave radiation at a maximum power of 800 W. The temperature was measured with a temperature sensor (type K thermocouple) inserted inside the vessel. Each as-prepared solution was subjected to microwave hydrothermal synthesis and heated to a temperature of 140 °C for 10 min. The products were then air-cooled to room temperature. The as-obtained precipitate powder was washed several times with distilled water and isopropyl alcohol and then dried on a hot plate at 60 °C for 24 h.

Characterization

The powder X-ray diffraction (XRD) characterization was performed using a Shimadzu diffractometer (Model XRD-7000, $\text{CuK}\alpha$ radiation ($\lambda=1.54$ Å), 40 kV and 30 mA). The scanning range was between 5 and 120° (2 θ), with a step size of 0.02° and a step time of 5.0 s. Rietveld analysis was performed using the Rietveld refinement program GSAS¹². A pseudo-Voigt profile function was used. The specific surface area (S_{BET}) was estimated from the N_2 adsorption/desorption isotherms at liquid nitrogen temperature following the multipoint BET procedure, using a Micromeritics ASAP 2000. Determination of the concentrations of europium in doped samples was performed by Inductively Coupled Plasma Optical Emission Spectrometry (ICP-OES), using an iCAP 6500 Duo ICP (Thermo Fisher Scientific, Cambridge, United Kingdom) spectrometer and RACID86 Charge Injector Device (CID) detector, with iTEVA operational software. The quantification of europium in the solutions was measured at the following emission wavelength: Eu II 381.967 nm. Morphology of the nanostructures was characterized by transmission electron microscopy (TEM) and by field emission scanning electron microscopy (FE-SEM). TEM characterization was conducted on Philips CM 300 microscope operating at 300 kV. The SEM measurements were carried out on a Tescan MIRA3 field emission gun, at 10 - 20 kV in high vacuum. SEM working distance was between 3.3 and 4 mm. Room temperature micro-Raman spectra of $\text{Pr}_{1-x}\text{Eu}_x(\text{OH})_3$ nanostructures were excited using solid state Nd:YAG laser line of 514 nm. Low laser power (~2 mW) was applied to prevent thermal degradation of the sample. Tri Vista 557 triple spectrometer coupled to the nitrogen-cooled CCD detector was employed for spectra collection at room temperature. X-ray photoelectron spectroscopy (XPS) measurements were performed using the PHI ESCA system equipped with a non-monochromatic Al X-ray source (1486.6 eV) with a hemispherical analyzer. The infrared transmission spectra (IR) were obtained on a Thermo Nicolet 6700 Fourier transform infrared spectrophotometer at room temperature. Diffuse reflectance spectra (DRS) were acquired using the Specord M40 Carl Zeiss spectrometer. Room temperature PL measurements were performed on a Spex Fluorolog spectrofluorometer using 340 nm excitation wavelength.

Photodegradation tests

The photocatalytic activity of $\text{Pr}_{1-x}\text{Eu}_x(\text{OH})_3$ nanostructures under UV light irradiation was evaluated by monitoring the decomposition of reactive orange (RO16) as a model pollutant. Batch type experiments were performed in an open thermostated cell (at 25 °C) equipped with a water circulating jacket to maintain the solution at room temperature. A mercury lamp (125 W) was used as a light source. The initial concentration of RO16 in an aqueous suspension was 50 mg/L and the working volume was 25 mL. Before the photocatalytic experiment, the cell was kept in dark for 60 min in order to achieve the adsorption-desorption equilibrium. At regular time intervals the aliquots were taken and the dye concentration was monitored by measuring the variation of the intensity of absorption peak at $\lambda_{\text{max}} = 494$ nm, using a Varian Super Scan 3 UV-vis spectrophotometer. The photocatalytic experiments were conducted at the natural pH of the RO16 dye (pH=4.7). In order to detect the formation of photogenerated hydroxyl radicals (OH^\bullet), photoluminescence (PL) measurements were performed using terephthalic acid, which is known to react with OH^\bullet radicals and produces highly fluorescent 2-hydroxyterephthalic acid. The experiment was conducted at ambient temperature and the photocatalyst was placed in an open thermostated cell filled with 20 mL of the 5×10^{-4} mol L^{-1} terephthalic acid in a diluted NaOH aqueous solution with a concentration of 2×10^{-3} mol L^{-1} . UV light source was used and a sampling was performed after 5, 10 and 15 min. PL spectra of the reaction solution, using excitation wavelength of 315 nm, were measured on a Spex Fluorolog spectrofluorometer system, following the changes of PL peak at 425 nm for which the 2-hydroxyterephthalic acid exhibits intense PL peak.

Results and discussion

Structural characterization of obtained $\text{Pr}_{1-x}\text{Eu}_x(\text{OH})_3$ ($x = 0, 0.01, 0.03, 0.05$) nanostructures was performed using XRD analysis and diffraction patterns are shown in Fig. 1. All diffraction peaks of as-synthesized samples can be perfectly indexed to the hexagonal $P_{63/m}$ space group (ICSD No 200487 or JCPDS No 83-2304)¹³. Secondary peaks (marked with *) on Fig. 1.) at 23.5 °, 33.9 ° and 43.7 °, were detected in Eu-doped samples and ascribed to KNO_3 that was formed from the precursors¹⁴. Lattice parameters (a , c),

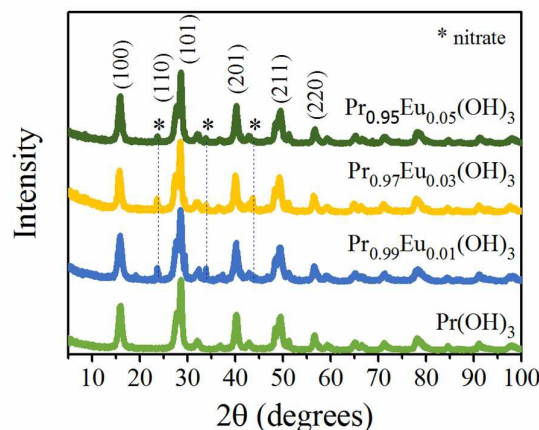


Figure 1. . XRD patterns obtained for $\text{Pr}_{1-x}\text{Eu}_x(\text{OH})_3$ nanostructures ($0 \leq x \leq 0.05$).

oxygen occupancy factor (O_{occup}) calculated from the Rietveld refinement and the quality factors (R_{exp} and R_{Bragg}) of the refinement are summarized in Table 1.

Positions of diffraction peaks assigned to KNO_3 are marked with asterisks. The lattice parameters slightly decreased with Eu doping due to the substitution of the larger Pr^{3+} ion (radii = 1.179 Å) by the smaller Eu^{3+} ion (radii = 1.12 Å)¹⁵, except for 3% Eu-doped sample. The decrease in O_{occup} with Eu doping signifies an increase in oxygen vacancy content. From Table 1 it can be seen that 3% Eu-doped sample has the smallest O_{occup} , i.e. the highest content of oxygen vacancies, the presence of which can be responsible for the observed lattice expansion in this sample¹⁶. In Table 1 are presented the BET specific surface area and the density of as-synthesized samples. Obviously, the specific surface area (S_{BET}) decreased in doped samples compared to the pure hydroxide, being the lowest in the 3% Eu-doped sample.

The type of dopant and its incorporation influence the properties of the obtained materials to great extent, therefore it is important to determine precisely the amount of the incorporated Eu in $\text{Pr}_{1-x}\text{Eu}_x(\text{OH})_3$ ($0.01 \leq x \leq 0.05$) nanopowders. In that sense, ICP analysis was performed and has shown that the content of incorporated Eu is a bit lower than its nominal content for each doped sample (see Table 2).

Table 1. Specific surface area (S_{BET}), lattice parameter (a and c), oxygen occupancy factor (O_{occup}) and density (ρ) of $\text{Pr}_{1-x}\text{Eu}_x(\text{OH})_3$ nanostructures.

Sample	S_{BET} ($\text{m}^2 \text{g}^{-1}$)	a (Å) ^a	c (Å) ^a	O_{occup} ^a	ρ (gcm^{-3}) ^a	R_{exp} (%)	R_{Bragg} (%)
$\text{Pr}(\text{OH})_3$	130.52	6.453(4)	3.769(9)	0.84(8)	4.45	11.6	6.0
1% Eu	83.24	6.453(4)	3.768(9)	0.80(2)	4.39	12.6	7.0
3% Eu	63.05	6.461(1)	3.769(0)	0.66(6)	4.22	13.0	8.5
5% Eu	82.77	6.449(0)	3.763(4)	0.74(5)	4.34	11.9	6.0

^a. Calculated via Rietveld refinement

ARTICLE

Table 2 Measured Eu content of $\text{Pr}_{1-x}\text{Eu}_x(\text{OH})_3$ nanostructures by ICP-OES.

Sample	Theoretical Eu content (mg/g)	Measured Eu content (mg/g)	Atomic concentration (%)
$\text{Pr}_{0.99}\text{Eu}_{0.01}(\text{OH})_3$	7.91	6.45	0.82
$\text{Pr}_{0.97}\text{Eu}_{0.03}(\text{OH})_3$	23.72	20.50	2.59
$\text{Pr}_{0.95}\text{Eu}_{0.05}(\text{OH})_3$	39.48	32.64	4.13

The morphology of pure and Eu-doped nanostructures was characterized by TEM and FE-SEM. In Fig. 2 are shown TEM images of pure and Eu-doped $\text{Pr}(\text{OH})_3$ nanostructures, whereas SEM images are shown in the Fig. S1 in the Supporting information. Pure $\text{Pr}(\text{OH})_3$ consists dominantly of well dispersed nanorods, with diameters ranging between 5 and 10 nm (Fig. 2(a)). With the increase of Eu dopant content, the morphology of the obtained nanomaterials changed and beside nanorods, the increasing presence of irregularly shaped grains that do not have nanorod morphology was also observed. This can be explained by the known fact that dopant atoms can change the crystallization directions and act as nucleation centers^{17, 18} thereby changing the resultant morphology of the sample. It is also worth to mention that in the case of 3% Eu-doped $\text{Pr}(\text{OH})_3$ sample two types of nanorods were formed – narrow ones with diameters in the range 7 - 15 nm (similar to pure $\text{Pr}(\text{OH})_3$) and wider ones, with diameters of the order of 50 nm (shown in the inset of Fig. S1(c)).

The nature of Eu ions incorporation was further studied by Raman spectroscopy, through the analysis of the influence that Eu doping has on the vibrational properties of the starting material, $\text{Pr}(\text{OH})_3$. Crystal symmetry of $\text{Pr}(\text{OH})_3$ is hexagonal, with symmetry group $P_{63/m}$, for which the group theory predicts 11 Raman active modes: 4 A_g , 2 E_{1g} and 5 E_{2g} modes^{19, 20}. In Fig. 3 are shown room temperature Raman spectra of pure and Eu-doped $\text{Pr}(\text{OH})_3$. Main Raman modes of $\text{Pr}(\text{OH})_3$ are present in the spectra of pure and doped samples and are positioned at energies: 140 cm^{-1} (peak 1), 240 cm^{-1} (peak 2), 294 cm^{-1} (peak 3), 359 cm^{-1} (peak 4), 465 cm^{-1} (peak 5). The modes positioned at 240 cm^{-1} and 294 cm^{-1} are ascribed to E_{1g} and E_{2g} lattice vibrations of OH^- anion, whereas E_{2g} lattice vibrational mode of heavier Pr^{3+} ions is positioned at lower energy of 140 cm^{-1} . Libration frequencies of OH^- atomic group are positioned at 359 cm^{-1} and 465 cm^{-1} (E_{2g} and E_{1g} modes)^{19, 20}. Raman peaks 3, 4 and 5 shifted slightly to higher wavenumbers in $\text{Pr}_{0.95}\text{Eu}_{0.05}(\text{OH})_3$ spectrum, which can be explained by a certain degree of Eu substitutional incorporation onto Pr sites, as these peaks are positioned at higher wavenumbers in $\text{Eu}(\text{OH})_3$ compared to $\text{Pr}(\text{OH})_3$ ²⁰. Several low-frequency modes at: ~ 53 cm^{-1} , ~ 85 cm^{-1} , ~ 107 cm^{-1} , ~ 127 cm^{-1} , and ~ 137 cm^{-1} are present in the Raman spectra of Eu-doped samples. These modes correspond to nitrates, either in the form of nitrate monohydrate layers interconnected with hydrogen bonds^{21, 22}, or in the form of KNO_3 ^{23, 24}, both of these compounds can be formed from unreacted nitrate ions originating from the precursor. Sharp Raman modes positioned at 715 cm^{-1} and

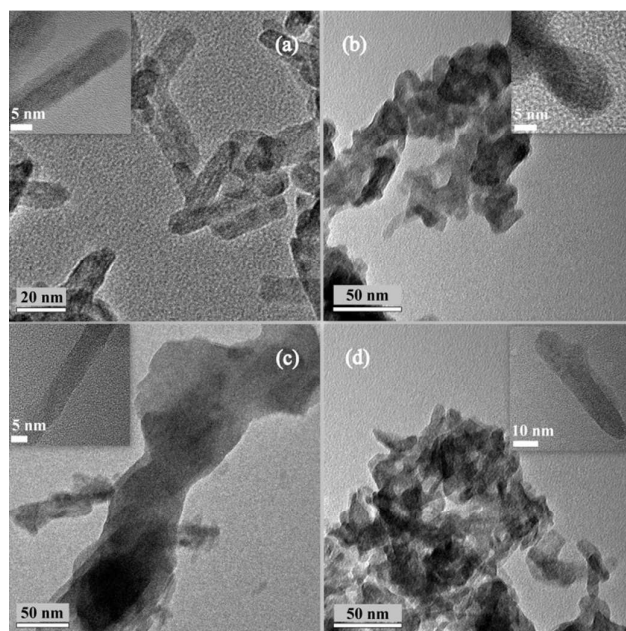


Figure 2. TEM images of (a) $\text{Pr}(\text{OH})_3$, (b) $\text{Pr}_{0.99}\text{Eu}_{0.01}(\text{OH})_3$, (c) $\text{Pr}_{0.97}\text{Eu}_{0.03}(\text{OH})_3$, (d) $\text{Pr}_{0.95}\text{Eu}_{0.05}(\text{OH})_3$ nanostructures. In the insets are shown magnified images of individual nanorods.

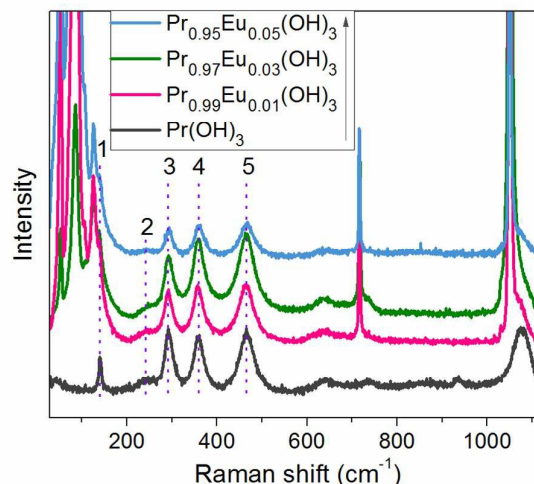


Figure 3. Room temperature Raman spectra of $\text{Pr}_{1-x}\text{Eu}_x(\text{OH})_3$ nanostructures.

1050 cm^{-1} correspond to the vibrations of NO_3^- ions^{23, 24}. Based on the results of Raman spectroscopy and having in mind X-ray diffraction results, we can conclude that some amount of crystalline KNO_3 phase is present in Eu-doped $\text{Pr}(\text{OH})_3$ samples. XPS measurements of $\text{Pr}_{1-x}\text{Eu}_x(\text{OH})_3$ samples enabled elucidation of changes in chemical composition and electronic structures with Eu doping and to determine the valence states of various species present in pure and doped samples.

Figure 4(a) shows the survey XPS spectra of $\text{Pr}_{1-x}\text{Eu}_x(\text{OH})_3$ samples whereas in Fig. 4(b) are shown Pr 3d, Eu 3d, O 1s and K 2p/C 1s XPS spectra. Pr 3d spectra (Fig. 4(b), upper left) contain two

spin-orbit doublets, labeled c/c' and b/b' , with approximate energies of 929/949 eV and 933/954 eV respectively. These doublets represent the $3d_{5/2}$ (c , b) and $3d_{3/2}$ (c' , b') components of the Pr $3d$ spectra. An additional structure t is present in the $3d_{3/2}$ component and can be explained by a multiplet effect. Doublets c/c' and b/b' are found both in Pr^{4+} and Pr^{3+} so they cannot be used to distinguish between these two valence states of Pr. Small peaks, observed at ~ 923 eV and ~ 943 eV, identified as X-ray satellites, originate from non-monochromatic X-ray source. From the Eu $3d$ spectra (Fig. 4(b), upper right) we can see that components Eu $3d_{5/2}$ and $3d_{3/2}$ are positioned at ~ 1134.7 eV and ~ 1164 eV. These values correspond to Eu^{3+} valence state. When compared to the literature values for Eu_2O_3 (1133.7)²⁵ $\text{Eu}(\text{OH})_3$ (1134.3)²⁶ and $\text{Eu}(\text{NO}_3)_3$ (1136.4)²⁵ it can be seen that these peaks are closest to those of $\text{Eu}(\text{OH})_3$ which confirms substitutional incorporation of Eu^{3+} and the absence of europium oxide/nitrate. One evidence more that Eu_2O_3

is not present in these samples is the fact that strong Raman mode of Eu_2O_3 at $\sim 330\text{ cm}^{-1}$ was not registered in the Raman spectra. K $2p$ states are particularly prominent in 1% and 3% Eu – doped samples (see Fig. 4(b)) and originate from KNO_3 phase, already seen in the XRD and Raman spectra of doped samples. Low intensity C $1s$ peak (see Fig. 4(b)) originates from surface impurity carbons, whereas N $1s$ states are characterized by very low intensity peaks visible in the survey XPS spectra. O $1s$ peaks of $\text{Pr}_{1-x}\text{Eu}_x(\text{OH})_3$ samples from Fig. 4(c) are asymmetric and have been deconvoluted into three components, positioned at ~ 529 eV, ~ 531 eV and ~ 532 eV, respectively. Vertical dashed lines shown in Fig. 4(c) indicate the binding energy (BE) position of the three components. The latter two are generally ascribed to lattice oxygen and adsorbed -OH groups, possibly from water²⁵⁻²⁷, whereas the peak at ~ 529 eV can be ascribed to the surface oxygen vacancies²⁰.

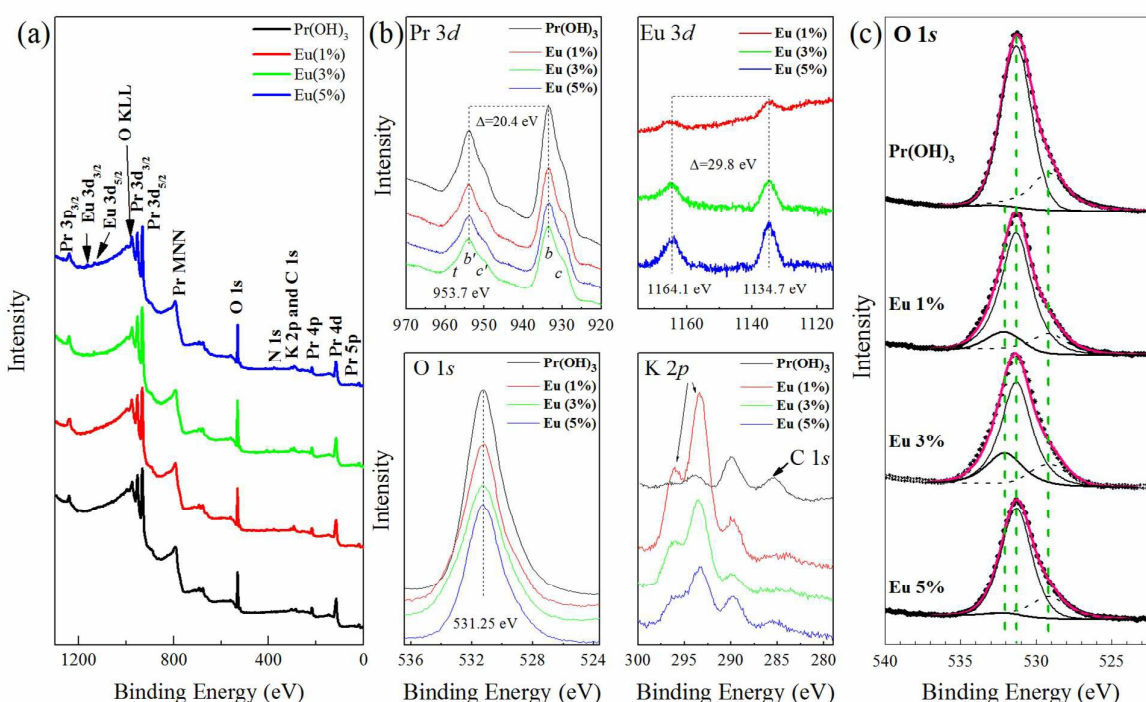


Figure 4. XPS spectra of $\text{Pr}_{1-x}\text{Eu}_x(\text{OH})_3$ nanostructures: (a) survey spectra (b) high-resolution spectra of Pr $3d$, Eu $3d$, O $1s$ and K $2p$ /C $1s$ regions and (c) deconvolution of O $1s$ region into three peaks.

Table 3. Elemental composition of $\text{Pr}(\text{OH})_3$, pure and Eu-doped as determined by XPS

Sample	Atomic concentration %				
	Pr	O	Eu	Eu/(Eu+Pr)	vacancy/lattice
$\text{Pr}(\text{OH})_3$	24.501	75.499	0.000		0.16
1% Eu	21.674	77.846	0.480	2 %	0.20
3% Eu	19.189	78.369	2.441	11.3 %	0.22
5% Eu	21.213	75.030	3.757	15 %	0.26

Elemental composition of the investigated samples, obtained by XPS measurements is represented in the Table 3. The following atomic concentrations, shown in Table 3, were obtained considering the sensitivity factors of PHI (Physical Electronics) and the peak features of Pr ($3d_{5/2}$), O ($1s$) and Eu ($3d_{5/2}$) from Fig. 4. It can be noticed, that relative atomic concentrations of Eu, calculated as $\text{Eu}/(\text{Eu}+\text{Pr})$ were higher than nominal stoichiometric concentrations of this element. This can be a consequence of the segregation of dopant atoms on the materials surface, already registered by XPS in other rare earths nanocomposites²⁸. This finding suggests that Eu^{3+} ions are segregated at the surfaces of

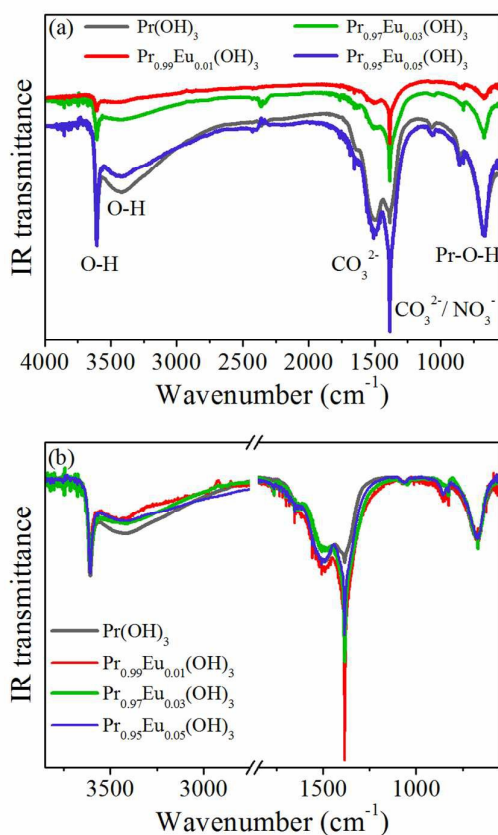


Figure 5. (a) IR transmission spectra and (b) Normalized IR spectra of pure and Eu-doped $\text{Pr}(\text{OH})_3$ nanostructures.

nanocrystals but mostly connected to oxygen ions as deduced from the Eu 3d binding energies. From the peak area fitting data of the components which belong to lattice oxygen and oxygen vacancies, we have calculated the oxygen molar ratio reported in Table 3 as well. Although XPS provides information about surface stoichiometry, the obtained ratio is in agreement with XRD results (see Table 1) confirming that Eu-doped samples are more oxygen deficient.

Infrared spectroscopy (IR) was employed to evidence the presence of -OH groups as well as other organic and inorganic species. IR transmission spectra of pure and Eu-doped $\text{Pr}(\text{OH})_3$, obtained in the range 500–4000 cm^{-1} are shown in Fig. 5. Peak at 670 cm^{-1} represents Pr-O-H lattice vibration^{13,20}.

Prominent broad peaks at 1382 cm^{-1} and 1505 cm^{-1} belong to symmetric and asymmetric COO^- vibrations²⁹, due to adsorbed carbon species. Another sharp peak at 1385 cm^{-1} , of much higher intensity in the spectra of doped samples, is observed. The sharp peak can be ascribed to NO_3^- vibrations³⁰ together with the observed low-intensity peak at $\sim 828 \text{ cm}^{-1}$, which also corresponds to NO_3^- vibrations and is present only in doped samples³⁰. The intensity of sharp peak (1385 cm^{-1}) is very high in 1% Eu – doped sample and decreases with the increase of dopant concentration, as shown in the normalized IR spectra from Fig. 5 (b) (normalized to

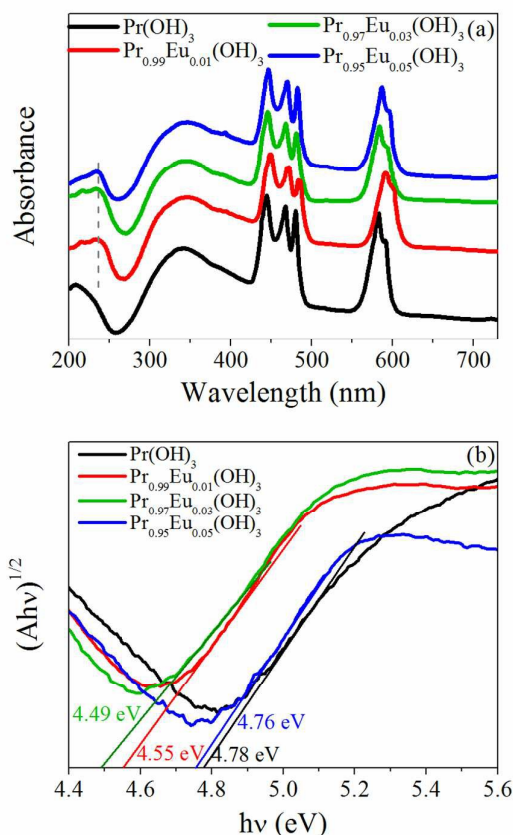


Figure 6. (a) Absorption spectra and (b) Tauc plots of $(Ah\nu)^{1/2}$ vs. $(h\nu)$ for $\text{Pr}_{1-x}\text{Eu}_x(\text{OH})_3$ nanostructures.

Pr-OH vibration peak), which is in agreement with XPS K 2p spectra of pure and doped samples. Another sharp peak at 3600 cm^{-1} represents the vibrations of OH⁻ groups from $\text{Pr}(\text{OH})_3/\text{Eu}(\text{OH})_3$ whereas broad peak at 3400 cm^{-1} corresponds to delocalized OH⁻ vibrations from adsorbed H_2O on the sample surface^{29,31}.

UV-vis absorption spectra of $\text{Pr}_{1-x}\text{Eu}_x(\text{OH})_3$ are presented in the Fig. 6(a). Strong absorption band can be observed in the region below 270 nm, corresponding to the band gap, and is shifted to lower wavelength for Eu-doped samples compared to $\text{Pr}(\text{OH})_3$ spectrum. Several sharper peaks at: 446 nm, 462 nm, 470 nm, 583 nm and 591–597 nm, represent Pr^{3+} electronic transitions. These peaks were observed in both pure and doped samples.

There are no peaks which can be ascribed to interband 4f–4f Eu^{3+} electronic transitions, due to the fact that the doping percentage is low. Another very broad absorption peak at $\sim 340 \text{ nm}$ can be ascribed to the formation of oxygen-vacancy impurity levels within the gap. These states are already seen in the defective $\text{La}(\text{OH})_3$ nanorods (absorption around 280 nm) and were ascribed to the surface oxygen vacancy states formed during the synthesis process³.

From the absorption spectra from Fig. 6(a), applying absorption spectra fitting method for indirect electronic transitions³², the band gap of these materials was estimated. In Fig. 6(b) are presented the

Tauc plots³³ for indirect transition for $\text{Pr}_{1-x}\text{Eu}_x(\text{OH})_3$ samples. It was deduced that the pure $\text{Pr}(\text{OH})_3$ band gap of ~ 4.78 eV is shifted to ~ 4.5 eV in $\text{Pr}_{0.99}\text{Eu}_{0.01}(\text{OH})_3$ and $\text{Pr}_{0.97}\text{Eu}_{0.03}(\text{OH})_3$, whereas it increases again in $\text{Pr}_{0.95}\text{Eu}_{0.05}(\text{OH})_3$ approaching the $\text{Pr}(\text{OH})_3$ value. The lower gap of 1% and 3% Eu-doped samples can be explained by the presence of higher amount of KNO_3 phase in these samples which has lower gap^{14,34} compared to $\text{Pr}(\text{OH})_3$.

In order to probe intraband defect states, PL measurements were performed using 340 nm excitation line with the purpose of exciting the states corresponding to the broad peak centered at 340 nm in the absorption spectra (see Fig. 6(a)). PL spectra of $\text{Pr}_{1-x}\text{Eu}_x(\text{OH})_3$ samples shown in Fig. S2 consist of an intense PL peak centered at 430 nm and several lower intensity Pr^{3+} emission peaks red-shifted compared to their counterparts in absorption spectra. The characteristic Eu^{3+} peaks are not seen, because of the presence of hydroxyl groups which act as luminescence quenching centers and can increase non-radiative processes³⁵. The intensive blue emission peak can be attributed to the deep level oxygen vacancy defect states and originates from the recombination of an electron occupying the vacancy and photogenerated holes^{3,36}. The intensity of this peak is increased in 3% and 5% Eu-doped samples. This is in accordance with XPS and XRD results from which was obtained that oxygen deficiency increased with increased Eu content.

Although the determined band gap values of $\text{Pr}_{1-x}\text{Eu}_x(\text{OH})_3$ nanostructures are relatively high, the sub band gap state observed from PL and UV-vis absorption spectra (see Figs. 6 (a) and S2) allows for these structures to be tested as potential photocatalysts in the UV region. Therefore, the photocatalytic degradation of RO16 dye was tested for $\text{Pr}_{1-x}\text{Eu}_x(\text{OH})_3$ nanostructures under UV light.

The kinetics of the degradation of RO16 under UV light is shown in Fig. 7(a). It is obvious that RO16 can be effectively removed by $\text{Pr}_{1-x}\text{Eu}_x(\text{OH})_3$ nanostructures. Pure $\text{Pr}(\text{OH})_3$ sample showed moderate adsorption in the dark and its photocatalytic removal efficiency was more than 90% after 180 minutes. Pronounced adsorption, in the equilibrium period of 60 min before the exposure to UV light, was seen in the 3% Eu-doped sample. On the contrary 1% and 5% Eu-doped samples showed no adsorption. The iso-electric point of a photocatalyst influences the adsorption process in great extent. Therefore, the zeta potentials for pure, 1% and 3% Eu-doped $\text{Pr}(\text{OH})_3$ (shown in Fig. 8(b)), were measured in the pH range 2.0-12.0 and the iso-electric points for these samples were 8.2, 7.6 and 8.8 respectively. At pH=4.7 which was the natural pH value of the solution, the surface charge of the catalysts is positive in the following order: 3% Eu > $\text{Pr}(\text{OH})_3$ > 1% Eu. As RO16 dye molecule is negatively charged the best adsorption is expected in 3% Eu-doped sample due to the stronger electrostatic interaction between the adsorbent and the adsorbate, little weaker adsorption is expected in $\text{Pr}(\text{OH})_3$ and the lowest in 1% Eu-doped $\text{Pr}(\text{OH})_3$ sample. This is in good agreement with the experimental results. The changes in morphology of 3% Eu-doped $\text{Pr}(\text{OH})_3$ (existence of two types of nanorods with diameters of the orders of magnitude ~ 10 nm and ~ 50 nm from Fig. S1(c)) and increased amount of oxygen vacancies (deduced from Rietveld analysis) in this sample can be additional reason for enhanced adsorption.

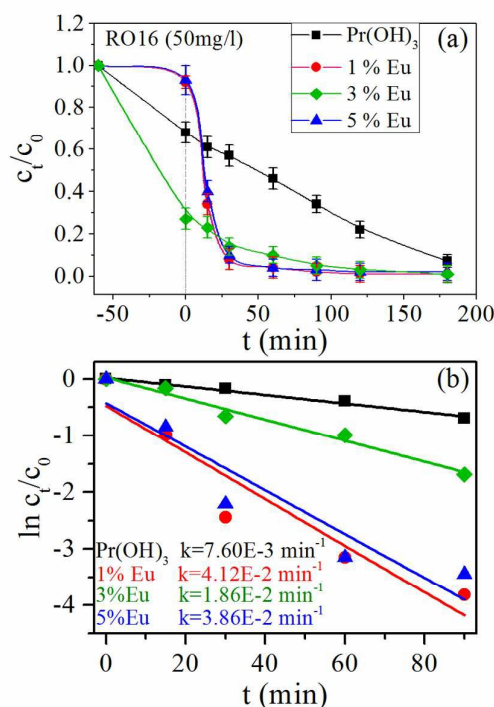


Figure 7. (a) Degradation of RO16 dye under UV light in the presence of pure and Eu-doped $\text{Pr}(\text{OH})_3$ nanostructures and (b) first-order reaction kinetics and constant k values.

Eu-doped $\text{Pr}(\text{OH})_3$ nanostructures exhibited much faster removal efficiency than pure $\text{Pr}(\text{OH})_3$ and exhibited faster dye removal at the beginning of the reaction time (Fig. 7(a)). Rapid removal of RO16 was observed in the first 30 minutes and after 70 minutes dye was almost completely removed. Under similar conditions, Eu-doped $\text{Pr}(\text{OH})_3$ nanostructures demonstrated even better photocatalytic activity than Degussa^{37,38}. Photocatalytic degradation of RO16 followed first-order kinetics (Fig. 7(b)), expressed by equation $\ln(C/C_0)=kt$, where C_0 is the initial dye concentration and C is the dye concentration at time t . The first-order rate constant k values, given by the slope of $\ln(C/C_0)$ vs. t , for $\text{Pr}_{1-x}\text{Eu}_x(\text{OH})_3$ samples are presented in Fig. 7(b). It can be deduced that Eu-doped samples have significantly higher k values than pure $\text{Pr}(\text{OH})_3$, confirming that these samples are better photocatalysts than pure $\text{Pr}(\text{OH})_3$ sample. XRD, XPS and UV-vis absorption spectra revealed that $\text{Pr}_{1-x}\text{Eu}_x(\text{OH})_3$ samples are oxygen deficient. Additionally, XRD results confirmed that the oxygen deficiency increases with Eu doping. XPS measurements suggested high segregation of Eu ions on the surface of doped nanostructures. The presence of lattice defects like oxygen vacancies (V_O) and Eu^{3+} ions, especially on the surface of Eu-doped nanostructures, can influence in great extent the photocatalytic activity of $\text{Pr}_{1-x}\text{Eu}_x(\text{OH})_3$ samples.

Photo-generated electrons or holes can be captured by V_O , which form impurity levels inside the gap and serve as charge carrier traps suppressing the e-h recombination process³⁹. On the other hand, the vacancies facilitate charge transfer to adsorption

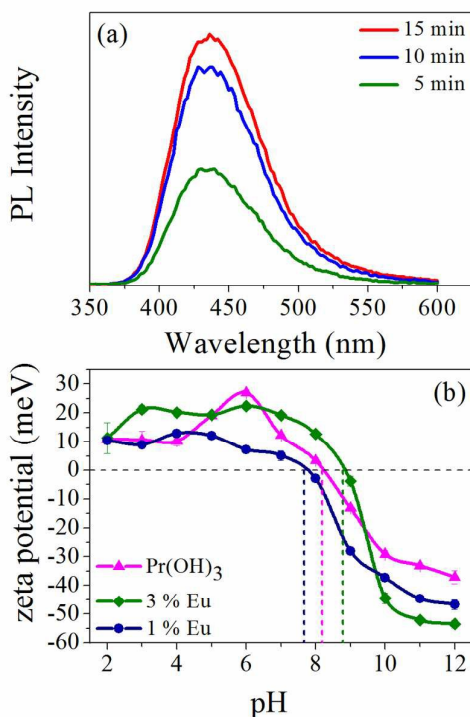


Figure 8. (a) PL spectral changes observed during UV illumination of $\text{Pr}_{0.95}\text{Eu}_{0.05}(\text{OH})_3$ sample in the solution of terephthalic acid after 5, 10 and 15 min. (b) Zeta potential dependence on pH value for pure, 1% and 3% Eu-doped $\text{Pr}(\text{OH})_3$.

species on the catalyst surface like O_2 or H_2O forming reactive radicals (superoxide radical ($\text{O}_2^{\bullet-}$) or OH^{\bullet}), the existence of which is important for fast and successful photocatalytic degradation of organic dyes. It is well documented that at the surface of oxide nanostructures like TiO_2 or CeO_2 , water dissociation takes place exclusively on oxygen vacancy defect sites where every surface V_O enables formation of two hydroxyl groups⁴⁰⁻⁴³. The infrared study of $\text{Pr}_{1-x}\text{Eu}_x(\text{OH})_3$ nanostructures confirmed the presence of hydroxyl groups from water.

The formation of OH^{\bullet} radicals was tested on the surface of $\text{Pr}_{0.95}\text{Eu}_{0.05}(\text{OH})_3$ photocatalyst under UV irradiation and detected by PL method. PL spectra of the reaction solution were measured at room temperature and these spectra are presented in Fig. 8(a). The terephthalic acid reacts with OH^{\bullet} radicals producing 2-hydroxyterephthalic acid, which exhibits PL peak at 425 nm⁴⁴. The intensity of this peak is proportional to the amount of OH^{\bullet} radicals produced in solution^{44, 45}. As can be seen from Fig. 8(a), substantial increase of the intensity of 425 nm peak with prolonged illumination time points to the increasing amount of OH^{\bullet} radicals produced at the surface of $\text{Pr}_{0.95}\text{Eu}_{0.05}(\text{OH})_3$ sample.

The existence of surface and subsurface vacancies also enables better adsorption of O_2 which can capture photogenerated electrons or electrons located on V_O , producing superoxide radical groups^{41, 46}. In addition to this, due to high oxidative potential of the

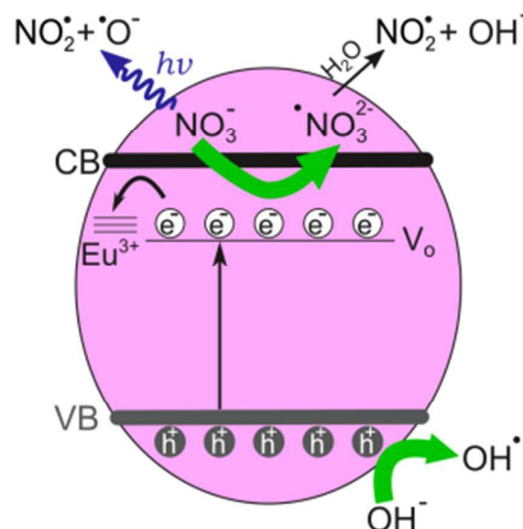
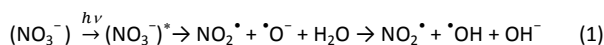


Fig. 9 Illustration of the photocatalytic mechanism of Eu-doped $\text{Pr}(\text{OH})_3$ under the UV light irradiation.

holes, holes can directly attack the dye leading to its oxidation ($\text{h}^+ + \text{dye} \rightarrow \text{dye}^{\bullet+} \rightarrow \text{oxidation of the dye}$). On the other side, the photogenerated holes can easily react with surface bound H_2O or hydroxyls (OH^-) forming hydroxyl radicals (OH^{\bullet}). Although similar studies, to the best of our knowledge, were not performed for $\text{Pr}(\text{OH})_3$ nanostructures, it is reasonable to assume that oxygen vacancies have important role in the photocatalytic process at the $\text{Pr}_{1-x}\text{Eu}_x(\text{OH})_3$ surface. Furthermore, recent papers of Dong et al.³ and Wang et al.¹¹ aimed at investigation of photocatalytic properties of defective $\text{La}(\text{OH})_3$ nanorods and $\text{La}(\text{OH})_3$ nanorods doped with 4f elements, demonstrated the crucial role of oxygen vacancies in the photocatalytic degradation of dyes and strongly supports our findings. The oxygen vacancy states in the band gap were registered by PL and absorption measurements.

On the other hand, Eu^{3+} ions are often used as dopants that can prevent quick recombination of photogenerated electrons and holes because they create surface states that present a barrier for electrons⁴⁷. The emission from these states was not observed in PL spectra excited with 340 nm, probably due to OH bond quenching, but since Eu^{3+} states were registered by XPS, they can be responsible for the enhanced photocatalytic activity of Eu-doped nanostructures due to the mentioned electron trapping effect.

In the recent paper of Mahlalela et al. it was demonstrated that TiO_2 nanoparticles exhibited enhanced photocatalytic activity in the presence of KNO_3 . This was ascribed to the increased production of hydroxyl radicals due to the presence of NO_3^- anions. The direct photolysis of nitrate ions (NO_3^-) during irradiation with $\lambda > 280$ nm can result in the formation of NO_2^{\bullet} and $\text{O}^{\bullet-}$ radicals. In the presence of water, $\text{O}^{\bullet-}$ radicals can be protonated giving hydroxyl radicals OH^{\bullet} and OH^- ions according to the following reaction⁴⁸:



In such a way the concentration of OH^\bullet radicals is increased enhancing the photodegradation of the dyes. On the other hand nitrate ions are good acceptors of photoinduced electrons forming nitrogen trioxide anion radicals ($^{\bullet}\text{NO}_3^{2-}$). These radicals in reaction with water form powerful nitrogen dioxide (NO_2^\bullet) anions, which are capable of oxidizing the dyes⁴⁸.

XPS, XRD and Raman analysis confirmed the presence of KNO_3 phase in Eu-doped samples. The presence of NO_3^- ions at the surface of doped samples can additionally improve their photocatalytic properties due to the mentioned radical formation. Considering all previously mentioned, a mechanism of photocatalytic reactions in Eu-doped $\text{Pr}(\text{OH})_3$ is proposed and presented in Fig. 9.

Photocatalytic stability was tested on the $\text{Pr}_{0.95}\text{Eu}_{0.05}(\text{OH})_3$ sample. Fig. S3 shows the repeated photocatalytic runs under the UV light irradiation. Although there was a certain drop in efficiency in the second run, these results indicated that Eu-doped $\text{Pr}(\text{OH})_3$ catalysts are stable after the second run. The drop in the efficiency after the first run is ascribed to the adsorbed dye molecules and reduction of number of active sites since the catalyst is recycled by centrifugation and deionized water washing, without additional chemical treatment.

Therefore enhanced photocatalytic activity of Eu-doped $\text{Pr}(\text{OH})_3$ nanostructures can be explained by the presence of oxygen vacancies, Eu^{3+} trapping states and KNO_3 -mediated hydroxyl radical production at the surface of our samples. Synergy of these three factors resulted in efficient separation of photogenerated electrons and holes and their transfer to adsorbed species at the surface enabling excessive formation of reactive radicals and efficient dye degradation.

This work provides new insight into the role of oxygen vacancies, 4f dopants and proper choice of alkaline metal hydroxides in promoting photocatalytic efficiency of $\text{Pr}(\text{OH})_3$. Our future work will be dedicated to the investigation of other 4f dopants influence on morphology, electronic structure and photocatalytic performances of $\text{Pr}(\text{OH})_3$ nanostructures.

Conclusions

In summary, defective $\text{Pr}_{1-x}\text{Eu}_x(\text{OH})_3$ nanostructures were synthesized by simple microwave-assisted hydrothermal method and comprehensive characterization has been performed by XRD, XPS, ICP-OES, FE-SEM, Raman, IR and DR spectroscopy. It was found that Eu^{3+} doping promotes the formation of oxygen vacancies and changes the morphology of $\text{Pr}(\text{OH})_3$ nanorods. Eu^{3+} ions have a tendency to segregate at the nanostructure's surface as well. Furthermore, the presence of KNO_3 phase is registered in doped samples. Eu-doped nanostructures exhibit excellent photocatalytic activity towards the photodegradation of an azo dye compared to pure $\text{Pr}(\text{OH})_3$ nanorods. Oxygen vacancies, change of morphology and presence of Eu^{3+} and NO_3^- ions at the $\text{Pr}(\text{OH})_3$ surface play significant role in improving the photocatalytic properties of $\text{Pr}(\text{OH})_3$ nanostructures. The enhanced photocatalytic activity of

$\text{Pr}_{1-x}\text{Eu}_x(\text{OH})_3$ nanostructures originates from combined effect of oxygen vacancies and Eu^{3+} ions, which act as trapping centres enabling at the same time facile charge transfer to adsorption species. In such a way fast electron hole recombination can be suppressed and more reactive radicals can be formed. The presence of KNO_3 phase in $\text{Pr}_{1-x}\text{Eu}_x(\text{OH})_3$ samples additionally improves the photocatalytic performances of $\text{Pr}(\text{OH})_3$ nanostructures, i.e. the presence of NO_3^- ions can enhance the production of NO_2^\bullet and OH^\bullet radicals. Furthermore, 3% Eu-doped sample exhibited very good adsorption properties due to higher electrostatic attraction of anionic dye and different morphology compared the rest of the samples. The possibility of tuning the ratio of photocatalytic versus adsorptive activity of Eu-doped $\text{Pr}(\text{OH})_3$ nanostructures makes them desirable for environmental applications.

Conflict of Interest

There are no conflicts of interest to declare.

Acknowledgements

This work was supported by Serbian Ministry of Education, Science and Technological Development under projects OI 171032 and III 45018. V. D. Araújo and M. I. B. Bernardi wish to thank Brazilian agencies FAPESP, FACEPE and CNPq for financial support. The authors wish to thank Prof Tamara Radetic for TEM images, Dr Aleksandar Matković and MSc Marijana Miličević for SEM images and to Dr Nenad Tadić for DRS measurements.

References

1. X. Wang and Y. Li, *Chemistry – A European Journal*, 2003, **9**, 5627-5635.
2. X. Ouyang, S. Yuan, Q. Qiu, W. Zeng, G. A. Hope and H. Li, *Inorg. Chem. Commun.*, 2014, **46**, 21-23.
3. F. Dong, X. Xiao, G. Jiang, Y. Zhang, W. Cui and J. Ma, *PCCP*, 2015, **17**, 16058-16066.
4. D. Zhang, T. Yan, L. Shi, H. Li and J. F. Chiang, *J. Alloys Compd.*, 2010, **506**, 446-455.
5. S. Zhang and C. Yao, *Mater. Lett.*, 2013, **94**, 143-146.
6. X. Sun, T. Zhai, X. Lu, S. Xie, P. Zhang, C. Wang, W. Zhao, P. Liu and Y. Tong, *Mater. Res. Bull.*, 2012, **47**, 1783-1786.
7. T. Zhai, S. Xie, X. Lu, L. Xiang, M. Yu, W. Li, C. Liang, C. Mo, F. Zeng, T. Luan and Y. Tong, *Langmuir*, 2012, **28**, 11078-11085.
8. J. Tang, J. Chen, W. Huang, D. Li, Y. Zhu, Y. Tong and Y. Zhang, *Chem. Eng. J.*, 2014, **252**, 202-209.
9. A. Dodd, *J. Colloid Interface Sci.*, 2013, **392**, 137-140.
10. X. Wang and Y. Li, *Angew. Chem. Int. Ed.*, 2002, **41**, 4790-4793.
11. Y. Wang, S. Liu, Y. Cai, S. Deng, B. Han, R. Han, Q. Li and Y. Wang, *Ceram. Int.*, 2014, **40**, 5091-5095.
12. A. C. Larson and R. B. Von Dreele, *Report LAUR 86-748*, Los Alamos National Laboratory, 2004.
13. D. F. Mullica, W. O. Milligan and G. W. Beall, *J. Inorg. Nucl. Chem.*, 1979, **41**, 525-532.
14. M. Hafez, I. S. Yahia and S. Taha, *Acta Phys. Pol., A*, 2015, **127**, 734-740.
15. R. Shannon, *Acta Crystallogr. Sect. A: Found. Crystallogr.*, 1976, **32**, 751-767.

ARTICLE

Journal Name

16. S. Deshpande, S. Patil, S. V. N. T. Kuchibhatla and S. Seal, *Appl. Phys. Lett.*, 2005, **87**, 133113.
17. J. D. Bryan and D. R. Gamelin, in *Prog. Inorg. Chem.*, John Wiley & Sons, Inc., 2005, DOI: 10.1002/0471725560.ch2, pp. 47-126.
18. C. Li, H. Liu and J. Yang, *Nanoscale Res. Lett.*, 2015, **10**, 1-6.
19. K. Ahrens, H. Gerlinger, H. Lichtblau, G. Schaack, G. Abstreiter and S. Mroczkowski, *J. Phys. C: Solid State Phys.*, 1980, **13**, 4545.
20. J.-G. Kang, Y. Jung, B.-K. Min and Y. Sohn, *Appl. Surf. Sci.*, 2014, **314**, 158-165.
21. R. M. Escibano, D. Fernández-Torre, V. J. Herrero, B. Martín-Llorente, B. Maté, I. K. Ortega and H. Grothe, *Vib. Spectrosc.*, 2007, **43**, 254-259.
22. H. Grothe, C. E. Lund Myhre and C. J. Nielsen, *J. Phys. Chem. A*, 2006, **110**, 171-176.
23. M. H. Brooker, *Can. J. Chem.*, 1977, **55**, 1242-1250.
24. D. Liu, F. G. Ullman and J. R. Hardy, *Phys. Rev. B*, 1992, **45**, 2142-2147.
25. F. Mercier, C. Alliot, L. Bion, N. Thromat and P. Toulhoat, *J. Electron. Spectrosc. Relat. Phenom.*, 2006, **150**, 21-26.
26. H. Wu, Y. Zhang, M. Zhou, C. Yao and X. Ge, *Cryst. Res. Technol.*, 2016, **51**, 508-512.
27. J.-C. Dupin, D. Gonbeau, P. Vinatier and A. Levasseur, *PCCP*, 2000, **2**, 1319-1324.
28. N. Paunovic, Z. Dohcevic-Mitrovic, R. Scurtu, S. Askrabic, M. Prekajski, B. Matovic and Z. V. Popovic, *Nanoscale*, 2012, **4**, 5469-5476.
29. J.-G. Kang, Y.-I. Kim, D. Won Cho and Y. Sohn, *Mater. Sci. Semicond. Process.*, 2015, **40**, 737-743.
30. J. T. Klopogge and R. L. Frost, *Journal*, 2001.
31. F. Cui, J. Zhang, T. Cui, S. Liang, L. Ming, Z. Gao and B. Yang, *Nanotechnology*, 2008, **19**, 065607.
32. N. Ghobadi, *Int. Nano Lett.*, 2013, **3**, 2.
33. M. Wang, P. Guo, T. Chai, Y. Xie, J. Han, M. You, Y. Wang and T. Zhu, *J. Alloys Compd.*, 2017, **691**, 8-14.
34. M. K. Aydinol, J. V. Mantese and S. P. Alpay, *J. Phys.: Condens. Matter*, 2007, **19**, 496210.
35. Z. Zuo, D. Liu, J. Liu, H. Liu, S. Qin and F. Zheng, *Mater. Chem. Phys.*, 2010, **123**, 502-506.
36. D. Liu, Y. Lv, M. Zhang, Y. Liu, Y. Zhu, R. Zong and Y. Zhu, *Journal of Materials Chemistry A*, 2014, **2**, 15377-15388.
37. D. Mijin, M. Radulović, D. Zlatić and P. Jovančić, *Chem. Ind. Chem. Eng. Q.*, 2007, **13**, 179-185.
38. R. C. Hsiao, L. S. Roselin, H.-L. Hsu, R. Selvin and R. S. Juang, *Int. J. Mat. Eng. Innov.*, 2011, **2**, 96-108.
39. F. Kayaci, S. Vempati, I. Donmez, N. Biyikli and T. Uyar, *Nanoscale*, 2014, **6**, 10224-10234.
40. R. Schaub, P. Thosttrup, N. Lopez, E. Lægsgaard, I. Stensgaard, J. K. Nørskov and F. Besenbacher, *Phys. Rev. Lett.*, 2001, **87**, 266104.
41. X. Pan, M.-Q. Yang, X. Fu, N. Zhang and Y.-J. Xu, *Nanoscale*, 2013, **5**, 3601-3614.
42. Z. Yang, Q. Wang, S. Wei, D. Ma and Q. Sun, *J. Phys. Chem. C*, 2010, **114**, 14891-14899.
43. N. M. Tomić, Z. D. Dohčević-Mitrović, N. M. Paunović, D. Ž. Mijin, N. D. Radić, B. V. Grbić, S. M. Aškrabić, B. M. Babić and D. V. Bajuk-Bogdanović, *Langmuir*, 2014, **30**, 11582-11590.
44. K.-i. Ishibashi, A. Fujishima, T. Watanabe and K. Hashimoto, *Electrochem. Commun.*, 2000, **2**, 207-210.
45. T.-M. Su, Z.-L. Liu, Y. Liang, Z.-Z. Qin, J. Liu and Y.-Q. Huang, *Catal. Commun.*, 2012, **18**, 93-97.
46. C. L. Muhich, Y. Zhou, A. M. Holder, A. W. Weimer and C. B. Musgrave, *J. Phys. Chem. C*, 2012, **116**, 10138-10149.
47. D. Yue, D. Chen, W. Lu, M. Wang, X. Zhang, Z. Wang and G. Qian, *RSC Advances*, 2016, **6**, 81447-81453.
48. L. C. Mahlalela and L. N. Dlamini, *Surf. Interfaces*, 2016, **103**, 21-28.